Photodissociation of O2 in the Herzberg continuum. I. Ab initio calculation of potential energy curves and properties

Mirjam C. G. N. van Vroonhoven and Gerrit C. Groenenboom

Citation: J. Chem. Phys. **116**, 1954 (2002); doi: 10.1063/1.1427714
View online: http://dx.doi.org/10.1063/1.1427714
View Table of Contents: http://jcp.aip.org/resource/1/JCPSA6/v116/i5
Published by the AIP Publishing LLC.

Photodissociation of O_2 in the Herzberg continuum. I. *Ab initio* calculation of potential energy curves and properties

Mirjam C. G. N. van Vroonhoven and Gerrit C. Groenenboom[a)]
Institute of Theoretical Chemistry, University of Nijmegen, Toernooiveld 1, 6525 ED Nijmegen, The Netherlands

(Received 24 July 2001; accepted 23 October 2001)

We present *ab initio* complete active space self-consistent-field plus multireference configuration interaction (CASSCF+MRCI) potential energy curves for the eight electronically excited ungerade states of oxygen ($A\ ^3\Sigma_u^+$, $c\ ^1\Sigma_u^-$, $A'\ ^3\Delta_u$, $^1\Pi_u$, $^3\Pi_u$, $^5\Pi_u$, $^5\Sigma_u^-$, and $2\ ^3\Sigma_u^+$) that correlate with the $O(^3P)+O(^3P)$ dissociation limit. We also report the R-dependent spin–orbit couplings between these states and the R-dependent radial derivative coupling matrix element $\langle 2\ ^3\Sigma_u^+|\partial/\partial R|\ A\ ^3\Sigma_u^+\rangle$. The near degeneracy in the long range of the same-symmetry states $2\ ^3\Sigma_u^+$ and $A\ ^3\Sigma_u^+$ may result in unphysical mixing of these states in a CASSCF calculation. We derive the correct asymptotic behavior of these states as dictated by the quadrupole–quadrupole interaction and we show how a correct long range description of these states can be achieved numerically by employing undistorted molecular orbitals. Bound state calculations using Herzberg I, II, and III potentials show excellent agreement with all available spectroscopic data. In the accompanying paper the potentials and couplings will be employed in a semiclassical study of the photodissociation of O_2 in the Herzberg continuum. © *2002 American Institute of Physics.* [DOI: 10.1063/1.1427714]

I. INTRODUCTION

The first step in the formation of ozone (O_3) in the atmosphere is the photodissociation of O_2.[1] Dissociation of ground state $O_2(X\ ^3\Sigma_g^-)$ occurs in the Herzberg continuum (200–240 nm) via transitions to the $A\ ^3\Sigma_u^+$, $c\ ^1\Sigma_u^-$, and $A'\ ^3\Delta_u$ states (the so-called Herzberg I, II, and III transitions). These three transitions are electric dipole forbidden and the photoabsorption cross sections are several orders of magnitude smaller than, e.g., the cross section in the Schumann–Runge continuum (below 176 nm) which arises from an allowed transition. Since the Herzberg continuum is very weak it allows sunlight to penetrate deep into the atmosphere where the O_2 concentration is large. As a result, the Herzberg transitions lead to 90% of the photodissociation of O_2 in the lower stratosphere and give rise to the Chapman ozone layer.[2,3]

In 1998 Buijsse *et al.*[4] constructed a photoabsorption model based on the latest experimental and theoretical knowledge of the Herzberg system. This model relies to a large extent on extrapolation of spectroscopic data for the Herzberg I, II, and III bands. These bands occur because the three electronically excited states are weakly bound. Note that in recent years several experimental studies reinvestigated these bands.[5–10] The Herzberg transitions borrow intensity from electric dipole allowed transitions, mainly through spin–orbit (SO) interactions in electronic ground and excited states. The Herzberg I transitions give the largest contribution to the Herzberg continuum. The dominant channels involve the $A\ ^3\Sigma_{u,\pm1}^+$ state ($\pm 73\%$ at $\lambda=226$ nm),

$$X\ ^3\Sigma_{g,\pm1}^- \overset{\parallel}{\rightarrow} B\ ^3\Sigma_{u,\pm1}^- \overset{\mathrm{SO}}{\leftrightarrow} A\ ^3\Sigma_{u,\pm1}^+,$$

$$X\ ^3\Sigma_{g,0^+}^- \overset{\mathrm{SO}}{\leftrightarrow} 1\ ^3\Pi_{g,0^+} \overset{\perp}{\rightarrow} A\ ^3\Sigma_{u,\pm1}^+,$$

and the $A\ ^3\Sigma_{u,0^-}^+$ state ($\pm 19\%$ at $\lambda=226$ nm)

$$X\ ^3\Sigma_{g,\pm1}^- \overset{\mathrm{SO}}{\leftrightarrow} 1\ ^3\Pi_{g,\pm1} \overset{\perp}{\rightarrow} A\ ^3\Sigma_{u,0^-}^+,$$

where the symbols $\parallel$ and $\perp$ refer to the parallel and perpendicular components of the dipole operator. The other transitions contributing to the Herzberg continuum are all perpendicular. A one-photon transition gives rise to an angular distribution of the photofragments $P(\theta)=1+\beta P_2(\cos\theta)$, where θ is the angle between the laser polarization and the fragment recoil direction and P_2 is the second order Legendre polynomial. In the sudden recoil limit the anisotropy parameter β equals 2 for a parallel transition and -1 for a perpendicular transition. Thus, Buijsse *et al.* could validate their photoabsorption model by determining the overall β parameter in an ion imaging experiment.

In this experiment[4] the atomic fragments were detected by (2+1) REMPI yielding $O(^3P_{j=2,1,0})$ fine-structure resolved, energy dependent anisotropy parameters $\beta_j(E)$. In the adiabatic (low energy) limit all the electronically excited states involved correlate with the $O(^3P_2)+O(^3P_2)$ limit. However, in the experiment $j=1$ and $j=0$ atomic fragments were found and furthermore the β_j parameters were different for $j=2$, 1, and 0. This suggests that initially excited states with different parallel/perpendicular character such as $A\ ^3\Sigma_{u,\pm1}^+$ ($\beta\approx 1.23$) and $A\ ^3\Sigma_{u,0^-}^+$ ($\beta=-1$) have different atomic fine-structure branching ratios. These branching ratios are determined by transitions that occur, as we will show, at interatomic distances between $R_{O-O}=4.5$ and 9 a_0

a)Author to whom correspondence should be addressed. Electronic mail: gerritg@theochem.kun.nl

where the separations between the potential energy curves correlating with the $O(^3P)+O(^3P)$ limit are of the same order as the spin–orbit couplings (≈ 1 mE_h). Thus the experimental results contain information about potentials and couplings in a region that is difficult to probe with spectroscopic techniques. In this paper we present *ab initio* calculations of the potentials and couplings for all eight ungerade states that correlate with the $O(^3P)+O(^3P)$ limit. The results are used in a dynamical calculation described in the accompanying paper,[11] where we compare calculated and measured $\beta_j(E)$ parameters.

In the experiment O_2 was prepared in a cold molecular beam, where the population of the ground state ($N=1$) was estimated to be at least 75%. Hence, we have ignored rotational couplings. We found, however, that in addition to the spin–orbit couplings, also the radial nonadiabatic coupling proportional to the nonadiabatic coupling matrix element (NACME) $\langle 2\,^3\Sigma_u^+|\partial/\partial R|A\,^3\Sigma_u^+\rangle$, which arises from the nonseparability of electronic and nuclear motion, becomes important between 4 and 8 a_0. The six ungerade states not involved in this coupling matrix element are all of different $D_{\infty h}$ symmetry, so all other radial derivative couplings are zero.

We will show that in the strong interaction region the CASSCF+MRCI method described in detail in Sec. III gives very good results by comparing (in Sec. V) calculated vibrational energy levels and rotational constants with spectroscopic data available for the Herzberg bands. However, this method gives convergence problems in the long range (see Sec. III). Furthermore, when the $A\,^3\Sigma_u^+$ and $2\,^3\Sigma_u^+$ states become nearly degenerate in the long range, they do not approach the correct atomic limit defined in Sec. II, but some (arbitrary) linear combination. This results in spin–orbit couplings not going to their analytically known long range values. Therefore we present an alternative procedure for obtaining molecular orbitals in the long range, also in Sec. III. In contrast to the CASSCF based calculations, this procedure gives the correct long range limit for the spin–orbit couplings. In Sec. II we derive this long range limit using the atomic spin–orbit coupling constant and angular momentum theory. We present the derivation in some detail because we will need the analytic description of the long range behavior of the electronic wave functions when we employ the *ab initio* results in the dynamical calculation in the accompanying paper.[11] In particular the relative signs of the couplings must be consistent. In Sec. IV we present fits of the potential curves that smoothly connect short range and long range results, and have the correct asymptotic behavior. We also present fits for the NACME and spin–orbit couplings. We will end with some conclusions in Sec. VI. Throughout this paper we employ atomic units. Note that 1 mE_h $=219.474\,63\ \mathrm{cm}^{-1}$.

II. THEORY

A. Potential energy curves

To describe the photodissociation of O_2, we calculated potential energy curves for all ungerade electronic states dissociating into two $O(^3P)$ atoms. Further we computed nonadiabatic and spin–orbit couplings between these states. The total Hamiltonian is given by

$$\hat{H}(R)=\hat{H}_{\mathrm{coul}}(R)+\hat{H}_{\mathrm{SO}}(R), \tag{1}$$

where $\hat{H}_{\mathrm{coul}}(R)$ is the usual time independent Coulombic Hamiltonian in the clamped nuclei approximation, $\hat{H}_{\mathrm{SO}}(R)$ is the spin–orbit interaction, and R is the internuclear distance. The potential energy curves $\epsilon_{c|\Lambda|S}(R)$ and the corresponding electronic adiabatic Born–Oppenheimer (ABO) wave functions are defined by

$$[\hat{H}_{\mathrm{coul}}(R)-\epsilon_{c|\Lambda|S}(R)]|c\Lambda S\Sigma;R\rangle=0, \tag{2}$$

where Λ, S, and Σ are the usual Hund's case (a) quantum numbers. The index c distinguishes between states that belong to the same irreducible representation of $D_{\infty h}$ and have the same spin part. All the electronically excited states that are relevant to our problem are ungerade and we omit this symmetry label. Upon dissociation into two Russell-Saunders coupled atoms the ABO wave functions can be expanded in products of atomic wave functions $|l_a\lambda_a\rangle|s_a\sigma_a\rangle|l_b\lambda_b\rangle|s_b\sigma_b\rangle$, or in coupled atomic states

$$|L\Lambda S\Sigma\rangle=|L\Lambda\rangle|S\Sigma\rangle, \tag{3}$$

with

$$\begin{aligned}|L\Lambda\rangle&=\sum_{\lambda_a\lambda_b}|l_a\lambda_a\rangle|l_b\lambda_b\rangle\langle l_a\lambda_a l_b\lambda_b|L\Lambda\rangle,\\ |S\Sigma\rangle&=\sum_{\sigma_a\sigma_b}|s_a\sigma_a\rangle|s_b\sigma_b\rangle\langle s_a\sigma_a s_b\sigma_b|S\Sigma\rangle,\end{aligned} \tag{4}$$

where a and b label the atoms, for $O(^3P)$ $l_a=l_b=s_a=s_b=1$, and λ_a, λ_b, σ_a, and σ_b are the projections of the atomic angular momenta on the internuclear axis. The symbol $\langle a\alpha b\beta|c\gamma\rangle$ is a Clebsch–Gordan coefficient. The coupling of l_a and l_b to L is not strictly necessary, but very convenient, since the ABO states will turn out to correlate in the long range one-to-one with these coupled atomic states.

If, for a given spin state and Λ quantum number, only one coupled atomic state $|L\Lambda S\Sigma\rangle$ exists it must correlate in the long range to an ABO state on symmetry grounds. Otherwise, we may construct long range ABO states by considering the leading interatomic term of the multipole expansion of $\hat{H}_{\mathrm{coul}}$ at large internuclear distance.[12] To find its matrix elements we write the interatomic potential part $\hat{V}$ of $\hat{H}_{\mathrm{coul}}$ as a multipole expansion in spherical tensor form.[13] With $K\equiv l_1+l_2$ we have

$$\hat{V}=\sum_{l_1 l_2}\frac{(-1)^{l_2}}{R^{K+1}}\left[\frac{(2K)!}{(2l_1)!(2l_2)!}\right]^{1/2}\hat{T}_K\equiv\sum_K\hat{V}_K, \tag{5}$$

with

$$\hat{T}_K=\sum_{m_1 m_2}\hat{Q}^{(a)}_{l_1 m_1}\hat{Q}^{(b)}_{l_2 m_2}\langle l_1 m_1 l_2 m_2|K0\rangle, \tag{6}$$

where we assumed the molecule to lie along the z axis. The Wigner–Eckart theorem relates the matrix elements of the atomic multipole operator $\hat{Q}^{(a)}_{l_1 m_1}$ to the reduced matrix element $\langle l_a \| \hat{Q}^{(a)}_{l_1} \| l'_a \rangle$,

$$\langle l_a m_a | \hat{Q}^{(a)}_{l_1 m_1} | l'_a m'_a \rangle = (-1)^{l_a - m_a} \begin{pmatrix} l_a & l_1 & l'_a \\ -m_a & m_1 & m'_a \end{pmatrix} \times \langle l_a \| \hat{Q}^{(a)}_{l_1} \| l'_a \rangle, \tag{7}$$

and similarly for atom b. We may also apply the Wigner–Eckart theorem to the coupled spherical tensor $\hat{T}_K$. Using the expression for its reduced matrix element (see, e.g., Eq. 5.68 in Ref. 14) we find

$$\langle (l_a l_b) L \Lambda | \hat{T}_K | (l'_a l'_b) L' \Lambda' \rangle = (-1)^{2K + L' - \Lambda'} \langle L \Lambda L', -\Lambda' | K 0 \rangle \begin{Bmatrix} l_a & l'_a & l_1 \\ l_b & l'_b & l_2 \\ L & L' & K \end{Bmatrix} \times \sqrt{(2L+1)(2L'+1)} \langle l_a \| \hat{Q}^{(a)}_{l_1} \| l'_a \rangle \langle l_b \| \hat{Q}^{(b)}_{l_2} \| l'_b \rangle. \tag{8}$$

The only permanent multipole moment of an O(^3P) atom is the quadrupole. The leading term of the interatomic potential is thus the quadrupole–quadrupole interaction $\hat{V}_5$, with $l_1 = l_2 = 2$ and $K = 4$. The $\hat{V}_5$ matrix elements are given by

$$\langle L \Lambda S \Sigma | \hat{V}_5 | L' \Lambda' S \Sigma \rangle = R^{-5} \delta_{L,L'} \delta_{\Lambda,\Lambda'} \tfrac{3}{2} \sqrt{70}\, Q^2_{zz} \times (-1)^{L - \Lambda} \langle L \Lambda L, -\Lambda | 4 0 \rangle, \tag{9}$$

where we define the quadrupole moment of O(^3P) as

$$Q_{zz} \equiv \langle 10 | \hat{Q}_{2,0} | 10 \rangle = -\sqrt{\frac{2}{15}} \langle 1 \| \hat{Q}_2 \| 1 \rangle. \tag{10}$$

Thus it turns out that the coupled atomic states correspond to long range ABO states, because the off-diagonal elements of V_5 are zero. Therefore we will drop the label c and instead use the notation $|(L)\Lambda S \Sigma; R\rangle$ for the ABO state computed at an interatomic distance R that correlates with $|L \Lambda S \Sigma\rangle$. In Table I we give for all ABO states relevant to our problem the usual spectroscopic notation, the corresponding quantum numbers L, $|\Lambda|$, and S, and the irreducible representation labels of D_{2h}, the group in which all numerical calculations were performed. The transformation between real D_{2h} adapted states and the complex spherical states $|(L)\Lambda S \Sigma; R\rangle$ is given by

$$\begin{aligned} |(L)\Lambda, x\rangle &= \frac{1}{\sqrt{2(1+\delta_{\Lambda,0})}} [(-1)^{\Lambda} |(L)\Lambda; R\rangle + (-1)^{L} |(L) -\Lambda; R\rangle], \\ |(L)\Lambda, y\rangle &= \frac{-i}{\sqrt{2(1+\delta_{\Lambda,0})}} [(-1)^{\Lambda} |(L)\Lambda; R\rangle - (-1)^{L} |(L) -\Lambda; R\rangle], \end{aligned} \tag{11}$$

where the spin part of the wave function $|S\Sigma\rangle$ has been omitted on both sides.

TABLE I. The labeling and the correlation with the coupled atomic states of the O_2 ungerade excited states. The coefficient c_0 denotes the fraction of $\lambda = 0$ atomic substates in the coupled atomic state, which is used in the BSSE correction, see Eqs. (17) and (18).

State	D_{2h}	$\|L\|\Lambda\|S\rangle$	c_0
$A\ ^3\Sigma_u^+$	$B_{1u}(x)$	$\|001\rangle$	1/3
$2\ ^3\Sigma_u^+$	$B_{1u}(x)$	$\|201\rangle$	2/3
$c\ ^1\Sigma_u^-$	$A_u(y)$	$\|100\rangle$	0
$^5\Sigma_u^-$	$A_u(y)$	$\|102\rangle$	0
$^1\Pi_u$	$\begin{Bmatrix} B_{2u}(y) \\ B_{3u}(x) \end{Bmatrix}$	$\|110\rangle$	1/2
$^3\Pi_u$	$\begin{Bmatrix} B_{2u}(y) \\ B_{3u}(x) \end{Bmatrix}$	$\|211\rangle$	1/2
$^5\Pi_u$	$\begin{Bmatrix} B_{2u}(y) \\ B_{3u}(x) \end{Bmatrix}$	$\|112\rangle$	1/2
$A'\ ^3\Delta_u$	$\begin{Bmatrix} A_u(y) \\ B_{1u}(x) \end{Bmatrix}$	$\|221\rangle$	0

B. Spin-orbit coupling

The Breit–Pauli spin–orbit Hamiltonian $\hat{H}_{\mathrm{SO}}(R)$ is given by[15]

$$\hat{H}_{\mathrm{SO}}(R) = \frac{g \mu_B^2}{c^2} \left(\sum_{i,n} \frac{Z_n \hat{\mathbf{s}}_i \cdot \hat{\mathbf{l}}^{(n)}_i}{r^3_{in}} - \sum_{i>j} \frac{2 \hat{\mathbf{s}}_i \cdot \hat{\mathbf{l}}^{(i)}_j + \hat{\mathbf{s}}_i \cdot \hat{\mathbf{l}}^{(j)}_i}{r^3_{ij}} \right). \tag{12}$$

In this formula the summation labels i and j indicate electrons and the label n runs over the nuclei. The symbol μ_B is the Bohr magneton, c is the speed of light, Z_n is the charge of nucleus n, $\hat{\mathbf{s}}_i$ is the spin operator for electron i, $\hat{\mathbf{l}}^{(a)}_i$ is the orbital angular momentum of electron i with respect to particle a (nucleus or electron), and r_{ab} is the distance between particles a and b. This Hamiltonian couples ABO states with the same value of $\Omega = \Lambda + \Sigma$. Matrix elements are nonzero for $\Delta\Omega = 0$, $\Delta\Lambda = -\Delta\Sigma = 0, \pm 1$, $\Delta S = 0, \pm 1$, $g \leftrightarrow g$, and $u \leftrightarrow u$. From the last two rules follows that we only need to consider the ungerade states, because the initial excitation is into the ungerade Herzberg system. Using the Wigner–Eckart theorem, the matrix elements of $\hat{H}_{\mathrm{SO}}(R)$ can be written as

$$\langle (L)\Lambda S \Sigma; R | \hat{H}_{\mathrm{SO}}(R) | (L')\Lambda' S' \Sigma'; R \rangle = (-1)^{S - \Sigma} \begin{pmatrix} S & 1 & S' \\ -\Sigma & m & \Sigma' \end{pmatrix} \times \langle (L)\Lambda S; R \| \hat{H}_{\mathrm{SO}}(R) \| (L')\Lambda' S'; R \rangle, \tag{13}$$

where $m = \Sigma - \Sigma'$ and the quantity between brackets is a $3j$ symbol. In the atomic region the spin–orbit coupling is given by

$$\hat{H}_{\mathrm{SO}}(\infty) = A(\hat{l}_a \cdot \hat{s}_a + \hat{l}_b \cdot \hat{s}_b), \tag{14}$$

where A is the atomic spin–orbit splitting constant, which has an experimental value of -0.353 mE_h for O(^3P) atoms.[16] For $R \to \infty$ we may also apply the Wigner–Eckart theorem to the orbital part to find an explicit expression for the reduced matrix element in Eq. (13),

$$\langle (L)\Lambda S;\infty \| \hat{H}_{\mathrm{SO}}(\infty) \| (L')\Lambda' S';\infty \rangle = 3A(-1)^{m+L-\Lambda} \begin{pmatrix} L & 1 & L' \\ -\Lambda & -m & \Lambda' \end{pmatrix} \times [R(s_a,s_b,S,S')R(l_a,l_b,L,L') + R(s_b,s_a,S,S')R(l_b,l_a,L,L')], \quad (15)$$

where the function $R(x_a,x_b,X,X')$ is given in terms of a $6j$ symbol by

$$R(x_a,x_b,X,X') = [(2X+1)(2X'+1)x_a(x_a+1)]^{1/2} \times (-1)^{x_a+x_b+X'} \begin{Bmatrix} x_a & x_a & 1 \\ X & X' & x_b \end{Bmatrix}. \quad (16)$$

Equation (15) can be used to illustrate one of the problems encountered in the long range with the standard CASSCF (+MRCI) method to calculate optimized MOs, properties and molecular energies (see Sec. III). If the wave functions for $A\ ^3\Sigma_u^+$ and $2\ ^3\Sigma_u^+$ do not converge to the correct atomic limits (with $L=0$ and $L=2$, respectively), but to an arbitrary linear combination, then the reduced matrix elements calculated on basis of these mixed wave functions will also tend to a linear combination of the values in the correct atomic limit.

III. CALCULATIONS

A. Potential energy curves

All calculations were performed with the MOLPRO[17] package. In the short range ($R<6\ a_0$) we use the augmented correlation consistent polarized valence quintuple zeta (aug-cc-pV5Z) one-electron basis set.[18] The orbitals were optimized with the CASSCF[19,20] method. In the calculations we employ D_{2h} symmetry, but $D_{\infty h}$ symmetry is imposed on the orbitals, using the LQUANT option. The states $A'\ ^3\Delta_u$, $A\ ^3\Sigma_u^+$, and $2\ ^3\Sigma_u^+$ appear all in the same B_{1u} irrep of D_{2h} (in this energy ordering at equilibrium geometry). The orbitals for $2\ ^3\Sigma_u^+$ are obtained in a state averaged calculation together with the $A\ ^3\Sigma_u^+$ and $A'\ ^3\Delta_u$ states. The orbitals for $A\ ^3\Sigma_u^+$ and $A'\ ^3\Delta_u$ are optimized in a state averaged calculation of only those two states. All other states are lowest in their symmetry and are optimized independently. The active space consists of all $2s$ and $2p$ valence orbitals and three extra bonding $[\sigma_g,\pi_u(x,y)]$ orbitals. The $1s$ core orbitals were fully optimized but kept doubly occupied.

The orbitals were used in an internally contracted multireference configuration interaction (MRCI)[21,22] calculation with single and double excitations. All configurations that contribute more than 1% to the CASSCF wave function are used as reference configurations in the MRCI calculation. The energies of the $A\ ^3\Sigma_u^+$ and $A'\ ^3\Delta_u$ states are calculated in a single calculation, optimizing both states simultaneously. The energy of the $2\ ^3\Sigma_u^+$ state is obtained by optimizing only the third B_{1u} state. We applied the Pople size consistency correction.[23] As we will show in Sec. V this method gives excellent results for the short range part of the potential.

However, for $R>6\ a_0$ we encountered three problems with this method.

(1) Convergence problems occurred in the CASSCF calculations in some cases.
(2) The reference configuration selection mechanism in the MRCI calculation results in discontinuities in the potential curves. The jumps are quite small ($\sim 200\mu E_h$), which is fully acceptable in the short range. In the long range, however, such jumps are not negligible compared to the interaction energies.
(3) The $A\ ^3\Sigma_u^+$ and $2\ ^3\Sigma_u^+$ state did not converge to the correct atomic limit. For example, the analysis in Sec. II shows that the SO coupling between $A\ ^3\Sigma_u^+$ and $^3\Pi_u$ should vanish for large R, whereas the reduced matrix element for the SO coupling between $2\ ^3\Sigma_u^+$ and $^3\Pi_u$ should be $\frac{3}{2}\sqrt{2}A$. However, at the CASSCF level these couplings are both nonzero (see Sec. V) suggesting that the computed states are linear combinations of the $A\ ^3\Sigma_u^+$ and $2\ ^3\Sigma_u^+$ states. This is of course not too surprising, since these states are of the same symmetry, and nearly degenerate for large R.

To circumvent these problems we employed a somewhat different approach for the long range calculations. For these calculations, we constructed molecular orbitals as fixed linear combinations of atomic orbitals. For instance, a $2p\pi_x$ orbital was constructed as $2p_x(A)+2p_x(B)$, etc. The atomic orbitals were determined in a separate state averaged CASSCF calculation of the three $O(^3P)$ states, which yields spherical symmetry adapted atomic orbitals. The active space in these calculations consisted of the $2s$ and $2p$ orbitals. In order to use the MOs in an MRCI calculation they were orthogonalized, but not optimized. First, core orbitals were constructed from atomic $1s$ orbitals. Then, the "active" space was constructed by projecting the core component out of the $2s/2p$ valence space. The virtual space was constructed as the orthogonal complement of the core and valence spaces. Within each orbital space orthonormal bases were obtained with Löwdin orthogonalization. In the MRCI calculation we used the complete active space as reference space, thus avoiding the discontinuities arising from configuration selection. In Sec. V we will demonstrate that these undistorted molecular orbital based calculations yield the correct atomic limit for the SO couplings. For these undistorted "long range" calculations we used a slightly smaller one-electron basis than for the short range. It consists of the $(13s8p)$ primitive set of van Duijneveldt,[24] which was contracted to $[5s4p]$ using the default MOLPRO contraction.[25] The primitive set was supplemented with a $(6d4f2g)$ even-tempered set of polarization functions with exponents of the form $\alpha=2.5^n\alpha_0$ with $\alpha_0=0.13$, 0.29, and 1.24 for the d, f, and g functions, respectively, and $n=0,\ldots,k-1$ where k is the number of functions in the set. These polarization functions were contracted to $[3d2f1g]$, again with the standard MOLPRO contraction. Finally a diffuse $s(\alpha=0.076\,666)$ and $p(\alpha=0.051\,556)$ orbital and the outermost $d(\alpha=0.13)$ orbital were added uncontracted.

B. Basis set superposition error

Extensive literature on van der Waals interactions shows that the Boys–Bernardi[26] counterpoise procedure is an effec-

tive method to reduce the basis set superposition error (BSSE).[27] van Mourik *et al.*[28] showed that for chemically bound diatomic molecules BSSE correction may improve the convergence behavior of molecular properties with basis set size, but that the corrected results are not necessarily in better agreement with the complete basis set limit than the uncorrected results. Hence, for the short range we minimized the BSSE by using a rather large one-electron basis. In the long range we used a BSSE correction. Note, however, that strictly speaking the Boys–Bernardi counterpoise procedure is not defined for a molecule dissociating into open-shell fragments. An ambiguity arises when the $O(^3P)$ atom is calculated in the molecular basis, because the cylinder symmetry of the molecular basis breaks the spherical symmetry of the atom. Specifically, the $O(^3P)$ states split into $\lambda=0$ and $|\lambda|=1$ states, where λ is the projection of the electronic orbital angular momentum on the internuclear axis. Fortunately, in the long range we can estimate the contributions from the atomic substates to the molecular wave functions using Eqs. (3) and (4). Thus, we generalized the Boys–Bernardi counterpoise procedure by defining the atomic energy for a given molecular state as the weighted average of the atomic substates, i.e.,

$$\Delta E_a(R)=c_0\Delta E_{\lambda=0}(R)+(1-c_0)\Delta E_{|\lambda|=1}(R), \tag{17}$$

with, for a molecular state $|L\Lambda S\Sigma\rangle$,

$$c_0=\sum_{\lambda_b}|\langle l_a 0 l_b \lambda_b|L\Lambda\rangle|^2 \tag{18}$$

and similarly for E_b. The value of c_0 is listed for all molecular states in Table I.

C. Couplings

We calculated the radial derivative couplings $\langle 2\,^3\Sigma_u^+|\partial/\partial R|A\,^3\Sigma_u^+\rangle$ with the two-point finite difference method ($\Delta R=0.1\ a_0$) as implemented in MOLPRO at the CASSCF as well as the CASSCF+MRCI level, and we repeated both calculations, using undistorted MOs. In these calculations we used the complete $2s/2p$ active space, and we employed the augmented Duijneveldt basis described above. In Sec. V we will argue that the results based on the undistorted long range method are to be preferred.

The spin–orbit matrix elements were calculated at the CASSCF level, taking into account both one- and two-electron integrals of the Breit–Pauli operator. Again the active space consisted of the $2s/2p$ orbitals. These calculations were also repeated using the long range method. As the one-electron basis we used the uncontracted $(12s6p3d)$ primitive Gaussians from the cc-pVQZ basis,[18] since the spin–orbit integral routines implemented in MOLPRO cannot handle contracted bases. A test calculation with the *s, p, d,* and *f* orbitals of the aug-cc-pV5Z basis resulted in a change of about 1%. The spin–orbit matrix elements being related by the Wigner–Eckart theorem [Eq. (13)], we only calculated the 21 independent reduced matrix elements listed below. Since the electronic wave functions were calculated separately at each geometry, the signs of the reduced matrix elements were not consistent between the different geometries. The signs were adapted so that all reduced matrix elements had smooth curves as function of *R*, and the same sign for $R=10.9\ a_0$ as in the atomic approximation given by Eq. (15).

IV. ANALYTIC FIT OF POTENTIALS AND COUPLINGS

A. Potential energy curves

Since we employ different methods in the short range and long range parts of the potential we must determine a relative energy shift of the two sets of *ab initio* points before we can fit the potential. The slopes of the potentials in the region where the data sets overlap do not match perfectly. Therefore, instead of matching the potentials in a single point, we leave a small gap between the short range and long range data sets and determine the relative shift by treating it as a free parameter in the fit. In this way we obtain a smooth fit. We use the functional form

$$V(R)=V_{\mathrm{SR}}(R)+V_{\mathrm{LR}}(R), \tag{19}$$

with

$$V_{\mathrm{SR}}(R)=\sum_{n=0}^{n_{\max}}\sum_{m=1}^{2}c_{n,m}y^n e^{-m\alpha y}, \tag{20}$$

where we introduced a shift $y=R-2.8$ for numerical reasons. Furthermore,

$$V_{\mathrm{LR}}(R)=\sum_{n=5,6,8,10}\frac{C_n^{(\mathrm{LR})}}{R^n}f_n(\beta R)+V_\infty, \tag{21}$$

where $C_5^{(\mathrm{LR})}$ accounts for the electrostatic quadrupole–quadrupole long range part of the potential and $C_6^{(\mathrm{LR})}$, $C_8^{(\mathrm{LR})}$, and $C_{10}^{(\mathrm{LR})}$ for dispersion. The functions f_n are Tang–Toennies damping functions[29]

$$f_n(x)=1-e^{-x}\sum_{k=0}^{n}\frac{x^k}{k!}. \tag{22}$$

We take $C_5^{(\mathrm{LR})}$ from Eq. (9), using the quadrupole moment of $O(^3P)$ of $Q_{zz}=-0.944\,64$ a.u. This quadrupole moment was calculated with MOLPRO, using a fourth-order finite field calculation (at field values $\pm 2.5\times10^{-4}$ and $\pm 5\times10^{-4}$ a.u.) with the partially spin–restricted open-shell single and double excitation coupled cluster method[30,31] with perturbative triples[32] [RCCSD(T)], employing a sextuple zeta (aug-cc-pV6Z)[33] basis set. We fix the long range coefficient $C_6^{(\mathrm{LR})}$ to the values listed for the various states by Dalgarno *et al.*[34] Note that the Q_{zz} value of -0.788 used in that paper is about 19% smaller than ours. That value was apparently calculated at the Hartree–Fock level. The long range coefficients $C_8^{(\mathrm{LR})}$ and $C_{10}^{(\mathrm{LR})}$ and V_∞ are determined in a linear least squares fit of $V_{\mathrm{LR}}(R)$ to the *ab initio* points in range 3 (given in Table II), with the damping function set to 1. A weighting of R^8 was used in this fit. After the long range parameters and V_∞ were determined in this way, all other parameters ($c_{n,m}$, α, β, and the relative energy shift) are found in a nonlinear least squares fit, with a weighting of R^3. The short range and long range data sets used in this final fit are given as range 1 and 2 in Table II, which also specifies the values of $n_{\max}$. The asymptotic value of the potentials is

TABLE II. Fit of the potential energy curves. Data points from the "short range" (Range 1) and "long range" (Range 2) calculations used in the fit, and "long range" method data points (Range 3) used in the fit of the coefficients $C_8^{(LR)}$ and $C_{10}^{(LR)}$, are given as $R_{min}-R_{max}$ (in a_0), where all points within the interval (the given values included) with a grid spacing of 0.1 a_0 have been used. The fit error in the short range part is given in the column headed "SR error" as the maximum absolute error for all points with $R \leqslant 8.0\ a_0$. The error in the long range is given in the last column as the largest relative error in the data points with $R > 8.0\ a_0$.

State	Range 1	Range 2	Range 3	n_{max}	SR error (μE_h)	LR error (%)
$c\ ^1\Sigma_u^-$	2.2–4.5	5.5–10.0	8.0–10.6	6	40	1.2
$A'\ ^3\Delta_u$	2.3–4.5	5.5–8.0	8.4–10.6	6	34	1.6
		8.7–10.6				
$A\ ^3\Sigma_u^+$	2.3–4.5	5.5–10.0	7.0–10.3	6	37	0.8
$^1\Pi_u$	3.0–5.9	7.7–10.3	8.5–10.3	5	35	0.8
$^3\Pi_u$	2.7–5.4	7.5–10.3	7.5–10.3	5	52	0.4
	5.7–6.5					
$^5\Pi_u$	3.0–6.0	7.5–10.3	8.0–10.3	5	23	1.1
$^5\Sigma_u^-$	2.6–5.8	7.0–10.6	8.4–10.6	6	65	1.7
$2\ ^3\Sigma_u^+$	3.7–4.3	4.6–10.0	7.0–11.0	4	17	0.4

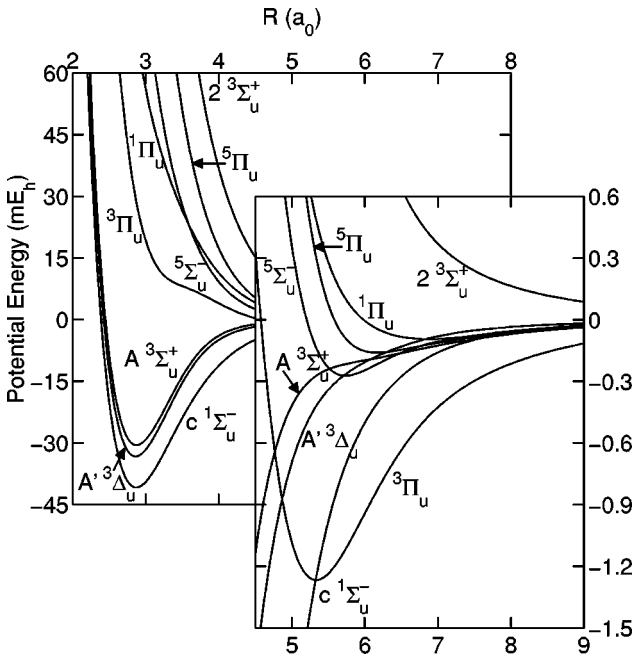

FIG. 1. Calculated potential energy curves for the ungerade states dissociating to $O(^3P)+O(^3P)$. Note that the potential axis on the right-hand side ($R \geqslant 4.5$) is scaled with a factor of 50 with respect to the left-hand side of the figure.

made equal by setting $V_\infty = 0$ for all states. The polynomials in the exponential part of the fit cause unphysical oscillatory behavior of the fit when it is extrapolated towards small R. To ensure physical behavior in the extrapolation we used an exponential function $C'\ \exp[-\alpha'(R-R'_{shift})]$, where C' and α' were chosen so that the value and derivative of this exponential match with the fitted curve at the innermost data point (at R'_{shift}). Fortran routines to evaluate the potential energy curves can be downloaded from the EPAPS service.[35]

B. Nonadiabatic coupling

The nonadiabatic coupling as a function of R consists of a single, somewhat asymmetric peak. The tails of the peak appear to go to zero faster than a Lorentzian and slower than a Gaussian function. We obtained a good fit with the functional form

$$g_{2,A}(R) = \frac{C_1}{1+C\{\exp[-\alpha_1(R-R_1)]+\exp[\alpha_1(R-R_1)]\}} + \frac{C_2}{1+C\{\exp[-\alpha_2(R-R_2)]+\exp[\alpha_2(R-R_2)]\}}. \tag{23}$$

It has two linear parameters, the peak heights C_1 and C_2, and five nonlinear parameters, the peak positions R_1 and R_2, the peak width parameters α_1 and α_2, and the parameter C that influences the shape of the peak. The nonlinear least squares fit employed a weighting function of $|g_{2,A}(R)|^{-1/2}$, i.e., a higher weight when the coupling is smaller. This fit procedure results in a relative error of 0.3% around the peak maximum. The relative error is smaller than 1% for $R \leqslant 9\ a_0$, and increases to 15% for $R = 11.0\ a_0$, where the coupling is only about 1% of its maximum. To compare the magnitude of the nonadiabatic coupling with the magnitude of the spin–orbit coupling, we have to multiply the nonadiabatic coupling by the dissociation fragment velocity v, which is given by $\sqrt{2E/\mu}$, where E is the kinetic energy, and μ is the reduced mass. At the highest experimental dissociation energy ($\lambda = 204$ nm, see the accompanying paper) we have an excess kinetic energy of 35 mE_h after dissociation. This corresponds to a fragment velocity of 2.2×10^{-3} atomic units. At the maximum of the peak of the nonadiabatic coupling, this corresponds to an energy $\hbar v \times \langle 2\ ^3\Sigma_u^+ | \partial/\partial R | A\ ^3\Sigma_u^+ \rangle = -0.43$ mE_h, which is comparable to the spin–orbit interaction (effective spin–orbit splitting constant $A = -0.36$ mE_h). At internuclear distances $R > 9.0\ a_0$, $\hbar v \langle \partial/\partial R \rangle < 0.03$ mE_h, which is much smaller than the spin–orbit interaction.

C. Spin–orbit coupling

The R dependence of the spin–orbit matrix elements does not suggest a simple functional form. Therefore we used cubic spline interpolation, and exponential extrapolation. For extrapolation $R \to \infty$ we fitted a function of the form $A + B\ \exp[-\alpha(R-R_{end})]$ through the "long range method" data points with $10.0 \leqslant R \leqslant R_{end} = 10.9\ a_0$. We determined α in a nonlinear optimization procedure, fitting the parameters A and B using linear least squares, with unit weights. The long range extrapolation was then shifted to pass exactly through the last data point. For inward extrapolation we fitted an exponential of the form $A' + B' \exp[2.5(R-R_{start})]$, so that the value in the first data point (R_{start}, see Sec. V B) matched the "short range method" value, and the derivative in the first data point matched the derivative of the line connecting the first two data points. The spline is defined by the extra conditions of the derivatives in the first and last data points. We used "long range method" data points for

TABLE III. Spectroscopic constants for the bound states. Experimental values for the Herzberg states are from Ref. 36 and the experimental values for the $^3\Pi_u$ state are from Ref. 7. Calculated literature values for the Herzberg and very weakly bound states are from Ref. 37.

	R_e (a_0)			ω_e (mE_h)			D_e (mE_h)		
State	Present	Expt.	Calc.	Present	Expt.	Calc.	Present	Expt.	Calc.
$A\ ^3\Sigma_u^+$	2.8735	2.8724	2.880	3.655	3.663	3.563	30.52	30.33	29.55
$A'\ ^3\Delta_u$	2.8602	2.8592	2.867	3.732	3.713	3.590	33.29	33.20	32.38
$c\ ^1\Sigma_u^-$	2.8693	2.8610	2.874	3.601	3.631	3.517	40.87	41.00	40.57
$^5\Sigma_u^-$	5.735		6.24	0.268			0.272		0.199
$^5\Pi_u$	6.168		6.58	0.164			0.160		0.182
$^3\Pi_u$	5.333	...[a]	5.65	0.422	0.31[b]	0.27	1.267	0.64	0.873
$^1\Pi_u$	6.876			0.089			0.095		

[a]A value for R_e is not given, only $r_0=5.84$ and $r_1=6.65\ a_0$.
[b]This is not ω_e but $\Delta G_{1/2}$.

$R \geqslant 4.5\ a_0$, and "short range" data points for $R \leqslant 4.0\ a_0$. Fortran routines to evaluate the spin–orbit and nonadiabatic coupling are also available from EPAPS.[35]

V. RESULTS AND DISCUSSION

A. Potential energy curves

In Fig. 1 we show the fits of the potential energy curves. In Table III we list the calculated spectroscopic constants R_e, ω_e, and D_e, together with experimental[36] and theoretical[37] literature values. For the three Herzberg states agreement of our results with experiment is excellent. For three of the four weakly bound states ($^5\Sigma_u^-$,$^5\Pi_u$,$^1\Pi_u$) no experimental data is available. The R_e values that we find for these states are about 0.5 a_0 shorter than the values computed by Partridge *et al.*[37] Our calculated R_e values are determined by our "short range" calculations which employ a larger one-electron basis as well as a larger number of active orbitals than the calculation by Partridge *et al.* The values that we find for the D_e of these weakly bound states in part depend on choices that were made when merging the short range and long range results.

The only spectroscopic data on the $^3\Pi_u$ state derives from its presumed role as perturber of the $A\ ^3\Sigma_u^+$ state.[7] It seems that our values for ω_e and D_e for this state are too large, while the results of Partridge seem closer to the experimental values (Table III). However, in the region of $R \sim 5-7\ a_0$ relevant for the observed $v=0$ and $v=1$ vibrational levels of the $^3\Pi_u$ state, the splittings between the ABO potentials are comparable to the spin–orbit coupling and one may not assume Hund's case (a) states. Preliminary calculations that take the SO coupling into account show a much better agreement with experiment when our potentials and SO couplings are used. We will analyze this matter in more detail in a separate paper.[38]

For the Herzberg states we calculated all the vibrational energies and rotational constants with the sinc-function discrete variable representation (sinc DVR) method.[39] In Tables IV, V, and VI we compare our results with the experimental values of Jenouvrier *et al.*[7] (where available) and Slanger.[36] Almost all errors are less than 1%. The most noticeable exceptions are the rotational constants of the highest vibrational levels, for which the errors are 1–2 orders of magnitude larger than for the other levels. This does not indicate a serious deficiency of our potentials. In fact, it can easily be understood because these energy levels are just below the

TABLE IV. Vibrational energies and rotational constants of all experimentally known vibrational levels of the $A\ ^3\Sigma_u^+$ state, compared with experimental data from Ref. 7 (where available) and 36.

v	$G(v)$ (mE_h)	Error (%)	$B(v)$ (μE_h)	Error (%)
0	1.809	−0.31	4.114	−0.24
1	5.330	−0.26	4.032	−0.30
2	8.712	−0.25	3.947	−0.33
3	11.944	−0.25	3.857	−0.34
4	15.011	−0.26	3.758	−0.36
5	17.897	−0.29	3.647	−0.41
6	20.576	−0.34	3.520	−0.50
7	23.021	−0.43	3.371	−0.66
8	25.195	−0.54	3.190	−0.92
9	27.050	−0.68	2.964	−1.26
10	28.532	−0.82	2.669	−1.43
11	29.588	−0.83	2.281	−0.83
12	30.199	−0.41	1.720	130

TABLE V. As Table IV, for the $c\ ^1\Sigma_u^-$ state.

v	$G(v)$ (mE_h)	Error (%)	$B(v)$ (μE_h)	Error (%)
0	1.784	−0.82	4.127	−0.55
1	5.260	−0.85	4.046	−0.74
2	8.606	−0.85	3.963	−0.58
3	11.818	−0.86	3.876	−0.59
4	14.891	−0.87	3.785	−0.60
5	17.819	−0.87	3.689	−0.61
6	20.596	−0.88	3.588	−0.63
7	23.217	−0.89	3.481	−0.64
8	25.674	−0.90	3.367	−0.63
9	27.964	−0.90	3.246	−0.66
10	30.079	−0.90	3.117	−0.63
11	32.016	−0.89	2.979	−0.58
12	33.770	−0.87	2.832	−0.48
13	35.337	−0.84	2.673	−0.34
14	36.714	−0.80	2.500	−0.21
15	37.895	−0.75	2.310	0.01
16	38.874	−0.70	2.096	0.28
17	39.645	−0.63	1.850	1.26
18	40.205	−0.51	1.567	5.45
19	40.566	−0.32	1.254	8.31

TABLE VI. As Table IV, for the $A'\ ^3\Delta_u$ state.

v	$G(v)$ (mE_h)	Error (%)	$B(v)$ (μE_h)	Error (%)
0	1.846	0.35	4.153	−0.26
1	5.440	0.20	4.073	−0.35
2	8.895	0.09	3.990	−0.34
3	12.202	−0.01	3.902	−0.38
4	15.351	−0.08	3.806	−0.39
5	18.326	−0.15	3.701	−0.41
6	21.109	−0.22	3.582	−0.49
7	23.675	−0.31	3.445	−0.63
8	25.995	−0.43	3.284	−0.84
9	28.033	−0.57	3.091	−1.17
10	29.749	−0.74	2.852	−1.56
11	31.106	−0.89	2.562	−1.63
12	32.098	−0.93	2.224	0.47
13	32.752	−0.76	1.826	46.2

dissociation limit, so that a small relative error in the vibrational energy may give a huge change in the expectation value of $\langle R^{-2}\rangle$.

In Fig. 2 we show the R dependence of the BSSE: $\Delta E_{\lambda=0}(R)$ and $\Delta E_{|\lambda|=1}(R)$ for the method that we used in the short range (solid lines) as well as for the method used in the long range (dashed lines). For both methods $\Delta E_{\lambda=0}(R)$ is larger than $\Delta E_{|\lambda|=1}(R)$, which is expected since the $\lambda=0$ component of the atomic O(^3P) state has two electrons in the p_z orbital (along the internuclear axis) in the dominant configuration, compared to one for the $|\lambda|=1$ components. Also we see that the short range calculation, which employs a larger one-electron basis gives a smaller BSSE. For the short range calculations the BSSE is about 1% of the D_e of the Herzberg states and we did not correct for this. Around 6 a_0 the BSSE for the long range calculation is in the order of 30% of the interaction and we applied the correction given in Eq. (17).

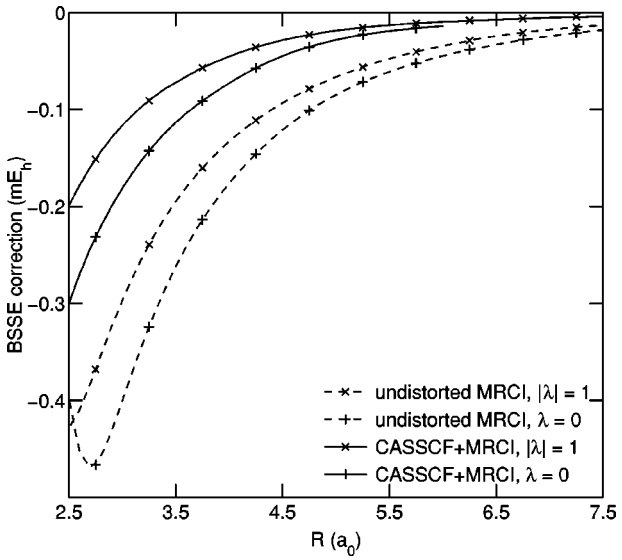

FIG. 2. The BSSE correction for the short range CASSCF+MRCI (solid lines) and long range undistorted orbitals MRCI calculation (dashed lines). The $\lambda=0$ (+ marks) and $\lambda=1$ (× marks) curves refer to atomic substates of Σ and Π symmetry.

TABLE VII. Spin–orbit reduced matrix elements $\langle(L)|\Lambda|S;R\|\hat{H}_{\rm SO}\|(L')|\Lambda'|S';R\rangle$ in μE_h. Quantum numbers L,Λ, and S for bra and ket states can be found in Table I. The atomic limit is calculated with the experimental splitting constant $A=-353\ \mu E_h$. The calculated values are for both the calculations for $R=7.5\ a_0$. *Ab initio* calculations were done between $R_{\rm start}$ and $10.9\ a_0$.

Number	bra	ket	$R_{\rm start}$ (a_0)	Atomic	LR method	SR method
1	$^1\Pi_u$	$A'\ ^3\Delta_u$	2.2	705	725	726
2	$^1\Pi_u$	$A\ ^3\Sigma_u^+$	2.2	−814	−815	−558
3	$^1\Pi_u$	$2\ ^3\Sigma_u^+$	3.7	288	355	693
4	$^3\Pi_u$	$A'\ ^3\Delta_u$	2.2	611	628	629
5	$^3\Pi_u$	$A\ ^3\Sigma_u^+$	2.2	0	−54	−405
6	$^3\Pi_u$	$2\ ^3\Sigma_u^+$	3.6	−748	−767	−656
7	$^5\Pi_u$	$A'\ ^3\Delta_u$	1.6	−789	−811	−813
8	$^5\Pi_u$	$A\ ^3\Sigma_u^+$	1.6	911	911	624
9	$^5\Pi_u$	$2\ ^3\Sigma_u^+$	3.5	−322	−396	−755
10	$^3\Pi_u$	$c\ ^1\Sigma_u^-$	1.6	499	513	514
11	$^3\Pi_u$	$^5\Sigma_u^-$	2.1	−558	−574	−575
12	$^5\Pi_u$	$^5\Sigma_u^-$	2.1	−966	−993	−995
13	$^1\Pi_u$	$^3\Pi_u$	2.2	499	513	511
14	$^3\Pi_u$	$^3\Pi_u$	2.2	−432	−444	−443
15	$^5\Pi_u$	$^3\Pi_u$	1.6	−558	−573	−572
16	$^5\Pi_u$	$^5\Pi_u$	2.2	−966	−994	−991
17	$A\ ^3\Sigma_u^+$	$c\ ^1\Sigma_u^-$	1.6	−814	−877	−1021
18	$2\ ^3\Sigma_u^+$	$c\ ^1\Sigma_u^-$	3.6	−576	−532	−64
19	$A'\ ^3\Delta_u$	$A'\ ^3\Delta_u$	1.8	−864	−889	−887
20	$A\ ^3\Sigma_u^+$	$^5\Sigma_u^-$	2.2	911	980	1141
21	$2\ ^3\Sigma_u^+$	$^5\Sigma_u^-$	3.8	644	594	71

B. Spin–orbit coupling

In Table VII we compare the reduced spin–orbit matrix elements calculated at $R=7.5\ a_0$ with the undistorted orbital method and with our ''short range method.'' We also list the asymptotic results corresponding to $A_{\rm exp}=-0.353$ mE_h. Generally, there is good agreement between the two calculated values and the experimental value, except when either the $A\ ^3\Sigma_u^+$ or the $2\ ^3\Sigma_u^+$ state is involved. In these cases the results for the ''short range method'' deviate considerably. We take this as an indication that the state-averaged CASSCF method, with the choice of the active space that we used in the short range, does not properly describe the nearly degenerate $A\ ^3\Sigma_u^+$ and $2\ ^3\Sigma_u^+$ states in the long range. Clearly, one expects the undistorted orbital method to fail somewhere in the strong interaction region. Fortunately, there is a region—as we show in Fig. 3—where both methods give nearly the same SO couplings, even when the $A\ ^3\Sigma_u^+$ or $2\ ^3\Sigma_u^+$ states are involved. This justifies our procedure of merging short range and long range results in the fit of the SO couplings.

In Figs. 4 and 5 we plot all the fits of the reduced matrix elements. We note that there is a considerable variation of the SO couplings with R. The fine-structure energy levels of the $A'\ ^3\Delta_{u,\Omega}$ state are given by $\epsilon_{v,\Omega}=\epsilon_{v,\Omega=2}+A_v\Lambda\Sigma$, where A_v is the effective spin–orbit coupling constant for vibrational level v. It is calculated as the expectation value of the R-dependent SO coupling $(1/2)\langle v|\langle(L=2)\Lambda=2,S=1,\Sigma=1;R|\hat{H}_{\rm SO}(R)|(L=2)\Lambda=2,S=1,\Sigma=1;R\rangle|v\rangle$ for the vibrational wave function of level v. Since different vibrational wave functions probe different R regions, the R dependence of the SO coupling is reflected in the variation of A_v with v.

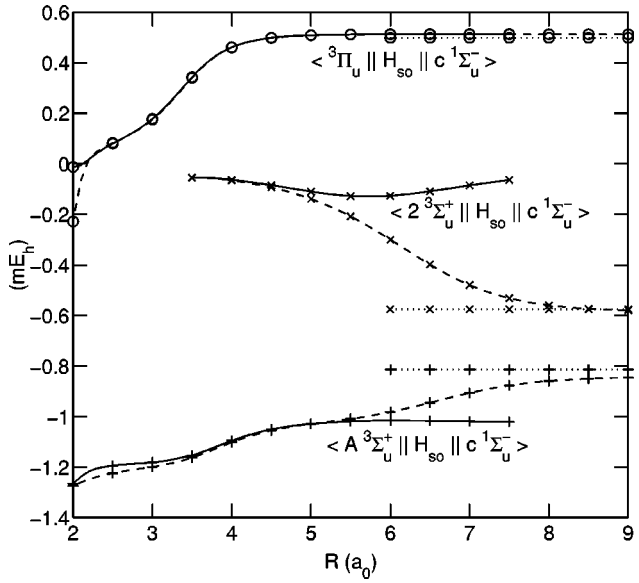

FIG. 3. Spin–orbit matrix elements $\langle A\ ^3\Sigma_u^+;R\|\hat{H}_{\mathrm{SO}}\|c\ ^1\Sigma_u^-;R\rangle$ (+ marks), $\langle 2\ ^3\Sigma_u^+;R\|\hat{H}_{\mathrm{SO}}\|c\ ^1\Sigma_u^-;R\rangle$ (× marks), and $\langle ^3\Pi_u;R|\hat{H}_{\mathrm{SO}}|c\ ^1\Sigma_u^-;R\rangle$ (o marks), calculated with optimized (solid lines) and undistorted atomic orbitals (dashed lines), and their analytic atomic limits (dotted lines).

In Table VIII we compare the calculated constants A_v with the experimental values from Refs. 36 and 40. Generally, the deviations from the experimental values are less than 4%. For $v=13$ the error is somewhat larger, which is of course consistent with the error found for the rotational constant for this level. We also compared our SO couplings with all the couplings between ungerade O_2 states that were calculated by Klotz and Peyerimhoff[41] and we found that all the differences are less than 15 μE_h.

At infinite separation, Eq. (15) relates all reduced spin–orbit matrix elements to a single atomic SO coupling constant A. We find that $A=-0.3627$ mE_h reproduces all fitted values at infinity to within 6.4 μE_h, and all nonzero values within 2%. A least squares fit of the eigenvalues of $A_{\mathrm{exp}}\hat{l}\cdot\hat{s}$ to the experimental atomic fine-structure levels[16] gives $A_{\mathrm{exp}}=-0.353$ mE_h. Note that the experimental energy levels do not exactly obey the Landé interval rule[42,43] due to spin–spin (and spin–other-orbit) interactions. In particular, $E_{j=1}-E_{j=2}=0.7222$ mE_h and $E_{j=0}-E_{j=2}=1.032$ mE_h, compared to $-2A_{\mathrm{exp}}=0.706$ mE_h and $-3A_{\mathrm{exp}}=1.059$ mE_h. Since we do not include spin–spin interactions that cause violation of the Landé interval rule, we cannot expect agreement with experiment to better than about 3%. In Table VII we also list R_{start}, the R value of the innermost data point. For smaller R, extrapolation has been used.

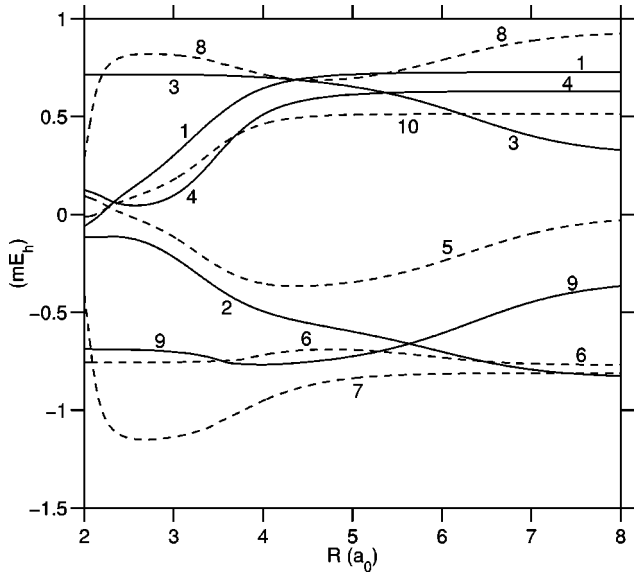

FIG. 4. Fits of the spin–orbit reduced matrix elements, numbers 1 to 10 from Table VII. The different line types are only to distinguish the different matrix elements.

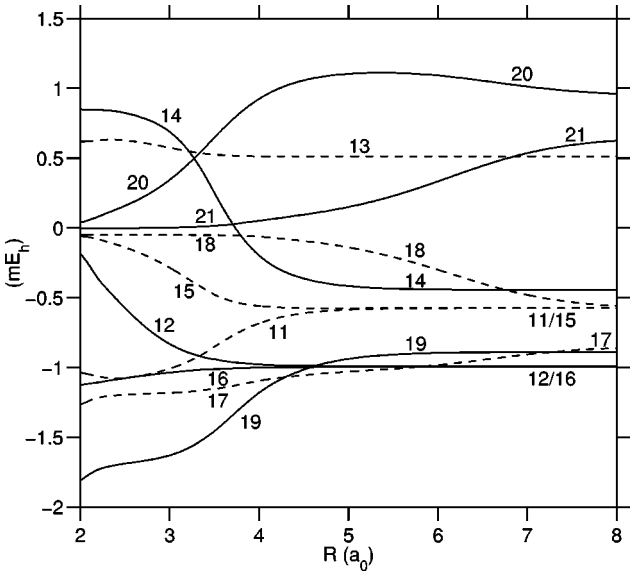

FIG. 5. As Fig. 4, numbers 11 to 21.

C. Nonadiabatic coupling

In Fig. 6 we plot the nonadiabatic coupling matrix element $\langle 2\ ^3\Sigma_u^+|\partial/\partial R|A\ ^3\Sigma_u^+\rangle$, calculated at the CASSCF (solid lines) and the MRCI (dashed lines) level employing both optimized (+ marks) and undistorted (× marks) orbit-

TABLE VIII. Calculated and experimental (Refs. 36 and 40) spin–orbit splitting constants (in mE_h) for the vibrational levels of $A'\ ^3\Delta_u$.

v	A_v calculation	A_v experiment	Error (%)
0	−0.3363	−0.3413	−1.47
1	−0.3344	−0.3401	−1.69
2	−0.3320	−0.3397	−2.27
3	−0.3292	−0.3377	−2.52
4	−0.3257	−0.3351	−2.80
5	−0.3214	−0.3316	−3.08
6	−0.3161	−0.3271	−3.38
7	−0.3092	−0.3211	−3.72
8	−0.3004	−0.3132	−4.08
9	−0.2891	−0.3020	−4.29
10	−0.2746	−0.2860	−3.99
11	−0.2570	−0.2630	−2.31
12	−0.2371	−0.2378	−0.28
13	−0.2163	−0.178	21.5

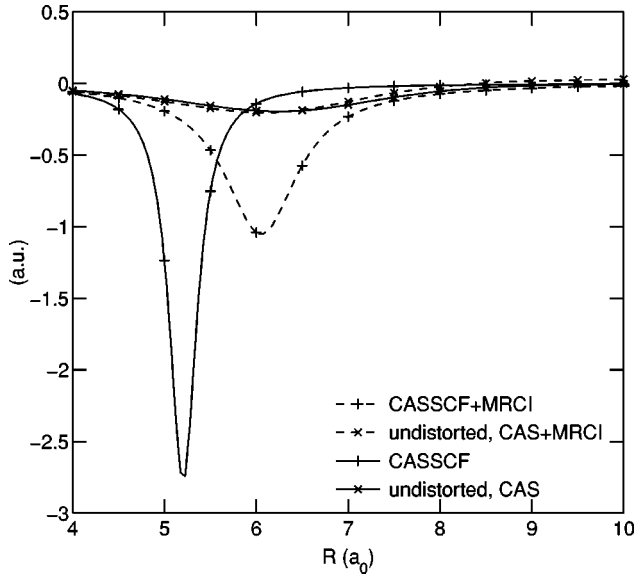

FIG. 6. The nonadiabatic coupling matrix element $\langle 2\,^3\Sigma_u^+|\partial/\partial R|A\,^3\Sigma_u^+\rangle$, as described in Sec. V C.

als. We find good agreement between these results in the region $R<4\ a_0$ where also the SO couplings match. For the optimized orbitals we find a very large coupling of −3 a.u. at $R=5\ a_0$. The MRCI calculation, employing these optimized orbitals gives rather different results, which one may take again as an indication that the optimized orbitals do not provide a good description of the $A\,^3\Sigma_u^+$ and $2\,^3\Sigma_u^+$ states in this region. By contrast, for the undistorted orbitals the MRCI results are very similar to the CAS results. In the fit we used the undistorted orbital CAS results.

VI. CONCLUSION

We performed high level *ab initio* calculations on the potential energy curves of several excited ungerade states of O_2: the Herzberg states $c\,^1\Sigma_u^-$, $A'\,^3\Delta_u$, and $A\,^3\Sigma_u^+$ and the repulsive states $^3\Pi_u$, $^1\Pi_u$, $^5\Sigma_u^-$, $^5\Pi_u$, and $2\,^3\Sigma_u^+$. We also calculated spin–orbit interactions between these states, and the nonadiabatic coupling matrix element $\langle 2\,^3\Sigma_u^+|\partial/\partial R|A\,^3\Sigma_u^+\rangle$. In the long range we used an approach based on undistorted atomic orbitals, to ensure that the states approach their correct atomic limit, defined by the quadrupole–quadrupole interaction, which is the first term in the multipole expansion of the interatomic potential. We combined these long range results with CASSCF optimized orbitals MRCI results employing an aug-cc-pV5Z AO basis. The resulting curves for the bound states reproduce all experimentally known vibrational levels within 1%, and rotational constants within 1% for all levels, except the very highest. The correctness of the atomic limit is necessary to obtain consistency in the nonadiabatic coupling matrix element and the spin–orbit matrix elements, that were also calculated as a function of the internuclear distance R. The nonadiabatic coupling was calculated in the same one-electron basis as the potential curves, the spin–orbit interaction in a smaller basis. We estimate the error in the spin–orbit matrix elements to be about 3%.

ACKNOWLEDGMENTS

The authors thank Ad van der Avoird and Paul E. S. Wormer for useful discussions and for carefully reading the paper. This research has been financially supported by the Council for Chemical Sciences of the Netherlands Organization for Scientific Research (CW–NWO).

[1] R. P. Wayne, *Chemistry of Atmospheres*, 2nd ed. (Clarendon, Oxford, 1991).
[2] D. H. Parker, Acc. Chem. Res. **33**, 563 (2000).
[3] S. Chapman, Mem. R. Meteorol. Soc. **3**, 103 (1930).
[4] B. Buijsse, W. J. van der Zande, A. T. J. B. Eppink, D. H. Parker, B. R. Lewis, and S. T. Gibson, J. Chem. Phys. **108**, 7229 (1998).
[5] M.-F. Mérienne, A. Jenouvrier, B. Coquart, M. Carleer, S. Fally, R. Colin, A. C. Vandaele, and C. Hermans, J. Mol. Spectrosc. **202**, 171 (2000).
[6] K. Yoshino, J. R. Esmond, W. H. Parkinson, A. P. Thorne, R. C. Learner, G. Cox, and A. S.-C. Cheung, J. Chem. Phys. **112**, 9791 (2000).
[7] A. Jenouvrier, M.-F. Mérienne, B. Coquart, M. Carleer, S. Fally, A. C. Vandaele, C. Hermans, and R. Colin, J. Mol. Spectrosc. **198**, 136 (1999).
[8] K. Yoshino, J. R. Esmond, W. H. Parkinson, A. P. Thorne, R. C. M. Learner, and G. Cox, J. Chem. Phys. **111**, 2960 (1999).
[9] J. P. England, B. R. Lewis, and S. T. Gibson, Can. J. Phys. **74**, 185 (1996).
[10] K. Yoshino, J. R. Esmond, J. E. Murray, W. H. Parkinson, A. P. Thorne, R. C. M. Learner, and G. Cox, J. Chem. Phys. **103**, 1243 (1995).
[11] M. C. G. N. van Vroonhoven and G. C. Groenenboom, J. Chem. Phys. **116**, 1965 (2002), following paper.
[12] S. J. Singer, K. F. Freed, and Y. B. Band, J. Chem. Phys. **79**, 6060 (1983).
[13] P. E. S. Wormer, F. Mulder, and A. van der Avoird, Int. J. Quantum Chem. **11**, 959 (1977).
[14] R. N. Zare, *Angular Momentum* (Wiley, New York, 1988).
[15] R. McWeeny, *Methods of Molecular Quantum Mechanics*, 2nd ed. (Academic, London, 1988).
[16] C. E. Moore, *Atomic Energy Levels as Derived From the Analysis of Optical Spectra*, Vol. I, No. 35, National Sandards Reference Data Series (National Bureau of Standards, Washington, DC, 1971).
[17] MOLPRO is a package of *ab initio* programs written by H.-J. Werner and P. J. Knowles, with contributions from J. Almlöf *et al.*
[18] T. H. Dunning, Jr., J. Chem. Phys. **90**, 1007 (1989).
[19] H.-J. Werner and P. J. Knowles, J. Chem. Phys. **82**, 5053 (1985).
[20] P. J. Knowles and H.-J. Werner, Chem. Phys. Lett. **115**, 259 (1985).
[21] H.-J. Werner and P. J. Knowles, J. Chem. Phys. **89**, 5803 (1988).
[22] P. J. Knowles and H.-J. Werner, Chem. Phys. Lett. **145**, 514 (1988).
[23] J. A. Pople, R. Seeger, and R. Krishnan, Int. J. Quantum Chem., Quantum Chem. Symp. **11**, 149 (1977).
[24] F. B. van Duijneveldt, IBM Research Report RJ945, 1971.
[25] The MOLPRO basis set library can be accessed online at http://www.tc.bham.ac.uk/molpro/molpro2000.1/molpro_basis
[26] S. F. Boys and F. Bernardi, Mol. Phys. **19**, 553 (1970).
[27] J. H. van Lenthe, J. G. C. M. van Duijneveldt-van de Rijdt, and F. B. van Duijneveldt, Adv. Chem. Phys. **69**, 521 (1987).
[28] T. van Mourik, A. K. Wilson, K. A. Peterson, D. E. Woon, and T. H. Dunning, Jr., Adv. Quantum Chem. **31**, 105 (1999).
[29] K. T. Tang and J. P. Toennies, J. Chem. Phys. **80**, 3726 (1984).
[30] P. J. Knowles, C. Hampel, and H.-J. Werner, J. Chem. Phys. **99**, 5219 (1993).
[31] P. J. Knowles, C. Hampel, and H.-J. Werner, J. Chem. Phys. **112**, 3106 (2000).
[32] J. D. Watts, J. Gauss, and R. J. Bartlett, J. Chem. Phys. **98**, 8718 (1993).
[33] A. K. Wilson, T. van Mourik, and T. H. Dunning, Jr., J. Mol. Struct.: THEOCHEM **388**, 339 (1997).
[34] B. Zygelman, A. Dalgarno, and R. D. Sharma, Phys. Rev. A **50**, 3920 (1994).
[35] See EPAPS Document No. E-JCPSA6-116-303204 for a Fortran implementation of the fit of the potential energy curves, spin–orbit couplings, and the radial derivative nonadiabatic coupling matrix element. This document may be retrieved via the EPAPS homepage (http://www.aip.org/pubserv/epaps.html) or from ftp.aip.org in the directory /epaps/. See the EPAPS homepage for more information.

[36] T. G. Slanger and P. C. Cosby, J. Phys. Chem. **92**, 267 (1988).
[37] H. Partridge, C. W. Bauschlicher, Jr., S. R. Langhoff, and P. R. Taylor, J. Chem. Phys. **95**, 8292 (1991).
[38] M. C. G. N. van Vroonhoven and G. C. Groenenboom (manuscript in preparation).
[39] G. C. Groenenboom and D. T. Colbert, J. Chem. Phys. **99**, 9681 (1993), note the mistake in the signs between the two terms in the first and second part of Eq. (48). See also D. T. Colbert and W. H. Miller, J. Chem. Phys. **96**, 1982 (1992).
[40] T. G. Slanger, D. L. Huestis, P. C. Cosby, H. Naus, and G. Meijer, J. Chem. Phys. **105**, 9393 (1996).
[41] R. Klotz and S. D. Peyerimhoff, Mol. Phys. **57**, 573 (1986).
[42] A. Landé, Z. Phys. **15**, 189 (1923).
[43] A. Landé, Z. Phys. **19**, 112 (1923).